Acoustic Signature Uncertainty Quantification for Quiet Supersonic Aircraft

Marian Nemec*
NASA Ames Research Center, Moffett Field, CA 94035, USA

Garo Bedonian†
Rensselaer Polytechnic Institute, 110 8th St, Troy, NY 12180, USA

Michael J. Aftosmis‡
NASA Ames Research Center, Moffett Field, CA 94035, USA

The goal of this work is to quantify uncertainty in the level of noise reaching the ground from supersonic aircraft at cruise conditions. To cope with uncertainty in the state of the atmosphere, the temperature and relative humidity profiles are parameterized using a Karhunen-Loève expansion based on a novel formulation involving dew point temperature. The noise statistics are evaluated with sparse quadratures. The flow simulations use nearfield-farfield domain decomposition. In the nearfield, the three-dimensional Euler equations are solved to obtain a pressure signature generated by the aircraft. In the farfield, this waveform is propagated to the ground by solving the augmented Burgers' equation. The use of sparse quadratures together with the domain decomposition approach enables efficient uncertainty assessment that minimizes the number of expensive nearfield simulations. The results show that truncating the Karhunen-Loève expansion after six terms is sufficient to model the atmospheric uncertainty accurately. This expansion is used in conjunction with uncertainty in flight conditions to estimate the ground noise statistics for the planned acoustic validation flights of the X-59 aircraft. We identify the atmosphere as the primary source of uncertainty, which causes dispersions in noise metrics of 4 to 8%. Furthermore, assuming a fixed aircraft weight and trim, no winds and ignoring the effects of atmospheric turbulence, the results show that the probability of satisfying a perceived level of loudness limit of 75 dB is 92%.

I. Introduction

Acoustic signatures of quiet supersonic aircraft are affected by many sources of uncertainty.[1–4] Perhaps the most obvious and concerning uncertainty stems from the propagation of pressure waveforms from the tropopause through a stratified and windy atmosphere to the ground. In particular, fluctuations in temperature, relative humidity and wind have a significant influence on the attenuation of the waveform, its arrival time, ground intercept and resulting noise.[5–8] The goal of this work is to characterize the effect of these uncertainties by efficiently estimating the mean and standard deviation of sonic-boom noise metrics.[9] In addition, by explicitly constructing the cumulative distribution function, we seek to estimate the probability of not exceeding specified noise limits due to supersonic cruise.

In previous work,[10] we investigated multilevel numerical quadratures coupled nonintrusively with high-fidelity simulations to characterize uncertainty in acoustic signatures of low-boom aircraft. The simulations used the standard nearfield-farfield domain decomposition approach illustrated in Fig. 1. The results show that in the nearfield, the probability density function of the pressure waveform is locally bimodal due to shocks. In contrast, the ground pressures of shaped signatures do not contain discontinuities, and we found

*Aerospace Engineer, Computational Aerosciences Branch, MS 258-5; marian.nemec@nasa.gov; Senior Member AIAA.
†Graduate Student, Department of Mechanical, Aerospace, and Nuclear Engineering; Student Member AIAA.
‡Aerospace Engineer, Computational Aerosciences Branch; michael.aftosmis@nasa.gov; Associate Fellow AIAA.

the waveform and noise metrics to be normally distributed. Hence, the mean and standard deviation statistics are sufficient to characterize the uncertainty in noise on the ground. These results were obtained using dense quadratures, which limited the problem size to fewer than five variables, such as Mach number, angle of attack, cruise altitude, the ground reflection factor and ground elevation.

The goal of this work is to efficiently handle uncertainty in the state of the atmosphere. Previous studies on the influence of atmospheric uncertainty on acoustic signatures[3,11–15] provide a limited statistical assessment. This is because they exclusively rely on measured profiles of the atmosphere or apply random perturbations about selected mean profiles. A promising multivariate surrogate approach is proposed by Lazzara *et al.*[6] that is based on altitude correlations and Monte Carlo sampling.

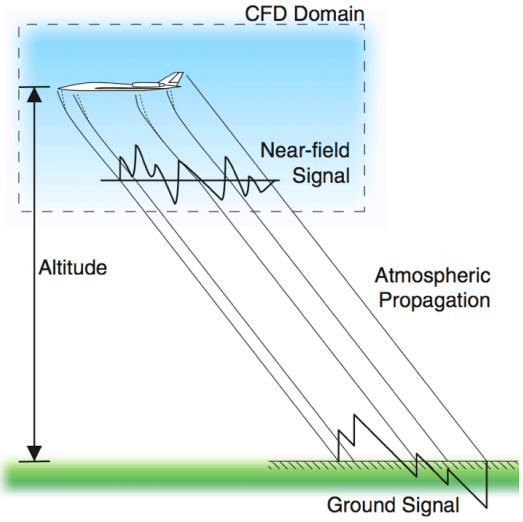


Figure 1: Sonic-boom domain decomposition

To develop a stochastic model of the atmosphere, we treat the temperature and relative humidity profiles as correlated, Gaussian-process random fields. We represent these fields using a truncated Karhunen-Loève (KL) expansion[16–18] that is based on the mean and covariance of a large dataset of measured profiles. This way the modeled temperature and relative humidity profiles are anchored to observations, and we obtain a parametric, low-dimensional model of the atmosphere. The main idea was proposed by Lorenz[19] in 1956, who applied it to modeling sea-level pressure at 64 stations in the US and Canada. More recently, similar approaches have been explored by Albert *et al.*,[20] who used KL expansions for atmospheric density fluctuations in planetary entry, and by Wang *et al.*[21] for stochastic wind models in flight safety applications. We introduce a novel formulation of modeling the temperature and relative humidity profiles through use of a dew point transformation. To control bias in the statistics, the simulations leverage discretization error control via adaptive mesh refinement in the combined nearfield-farfield domain.[22]

The results are presented in two parts. In the first part, we validate the KL expansion of atmospheric profiles by using comparisons with historical observations over the past twenty years at Edwards Air Force Base, California. Edwards is of particular interest — not only have many sonic-boom tests occurred there, but also it is the location for the planned acoustic validation flights of the X-59.[23] We study the number of variables required in the KL expansion to match the statistics of the observed profiles. In the second part, we demonstrate efficient uncertainty quantification in noise predictions on a realistic test case based on the X-59 aircraft, accounting for randomness in flight and atmospheric conditions.

II. Problem Formulation and Governing Equations

To compute the level of noise reaching the ground, the problem domain is divided into overlapping nearfield Ω_{N} and farfield Ω_{F} regions, as illustrated in Fig. 1. In the nearfield, we solve the steady, three-dimensional Euler equations governing compressible flow of a perfect gas to determine the nearfield pressure signature. For a finite region of space with volume V and surface area A, the integral form of the Euler equations is given by

$$\frac{\mathrm{d}}{\mathrm{d}t}\int_V \vec{\mathbf{Q}}\,\mathrm{d}V + \oint_A \bar{\mathbf{F}}\cdot\hat{\mathbf{n}}\,\mathrm{d}A = \mathbf{0} \tag{1}$$

where $\vec{\mathbf{Q}} = [\rho, \rho\vec{\mathbf{U}}, \rho\mathcal{E}]^{\mathrm{T}} = [\rho, \rho u, \rho v, \rho w, \rho\mathcal{E}]^{\mathrm{T}}$ are the non-dimensional conserved variables, and

$$\bar{\mathbf{F}}\cdot\hat{\mathbf{n}} = \begin{bmatrix} \rho U_{\mathrm{n}} \\ \rho U_{\mathrm{n}}\vec{\mathbf{U}} + p\hat{\mathbf{n}} \\ (\rho\mathcal{E}+p)U_{\mathrm{n}} \end{bmatrix} \tag{2}$$

where $U_{\mathrm{n}} = \vec{\mathbf{U}}\cdot\hat{\mathbf{n}}$ and $\hat{\mathbf{n}}$ is the outward facing unit normal. In the farfield, the evolution of the nearfield waveform as it descends through a stratified and windy atmosphere to the ground is modeled using geometric

acoustics in conjunction with the augmented Burgers' equation[24–26]

$$\frac{\partial P}{\partial \varsigma} = \frac{1}{2}\frac{\partial P^2}{\partial \tau} + \frac{1}{\Gamma}\frac{\partial^2 P}{\partial \tau^2} + \sum_{\nu} C_\nu \left(1 + \theta_\nu \frac{\partial}{\partial \tau}\right)^{-1} \frac{\partial^2 P}{\partial \tau^2} - \frac{P}{2S}\frac{\partial S}{\partial \varsigma} + \frac{P}{\rho_0 c_0}\frac{\partial(\rho_0 c_0)}{\partial \varsigma} \tag{3}$$

where $P = \frac{p_0}{p_r} p'$ is a pressure perturbation p' scaled by the ratio of local ambient and reference pressures. Equation 3 is in non-dimensional form and is solved in the (ς, τ) domain, where ς is the distance along a ray path between the aircraft and the ground, and τ is the retarded time along the signature. C_ν is the dispersion parameter, Γ the thermoviscous parameter, θ_ν the molecular-relaxation time parameter of the ν^{th} relaxation process, ρ_0 and c_0 the local density and speed of sound, respectively, and S the ray tube area.

Equations 1 and 3 are coupled at a boundary condition located a few body lengths away from the aircraft

$$P(\varsigma = A_\text{c} - L_\perp, \tau) = p'(\mathbf{x}) \quad \mathbf{x} \in \ell \in \Omega_\text{N} \tag{4}$$

where A_c is the cruise altitude, $L_\perp$ is the normal distance between the aircraft's flight path and the location of the line sensor ℓ that is used to extract the pressure signature $p' = (p - p_\infty)/p_\infty$ from Ω_N. Note that $L_\perp \ll A_\text{c}$ and that the steady pressure signature along ℓ initializes the propagation in the time domain, i.e., along τ, based on the cruise Mach number of the aircraft.

The primary output quantities of interest are the ground pressure signature and loudness metrics, namely the various weightings of the sound exposure levels (A/B/C/D/E-SEL [dB]), the perceived level of loudness (PL [dB]) and the Indoor Sonic Boom Annoyance Predictor (ISBAP [dB]).[9] These are not only evaluated directly under the flight path (on-track), as indicated in Fig. 1, but also off-track to determine the full sonic-boom carpet.[1,9]

To characterize uncertainty in an output, J, such as PL, we seek to determine the expectation (mean) and variance (square of standard deviation) statistics. Let ξ denote an input random variable of the simulation, e.g., uncertainty in cruise Mach number, that is distributed by a probability density function $f(\xi)$. The expectation is given by

$$E[J(p(x,\xi))] = \int J(p(x,\xi)) f(\xi) d\xi \tag{5}$$

where we emphasize the dependence of the functional J on the pressure signature $p(x,\xi)$ and note that J may be a scalar, e.g., a loudness metric, or a vector, e.g., a pressure signature. The variance and standard deviation are given by

$$V[J] = \sigma^2[J] = \int (J - E[J])^2 f(\xi) d\xi \tag{6}$$

Furthermore, we seek to characterize the uncertainty in J by estimating its probability density function p

$$\text{Prob}[a \le J \le b] = \int_a^b p(\xi) d\xi \tag{7}$$

and the cumulative distribution function

$$F_J(a) = \text{Prob}\left(J \le a\right) \tag{8}$$

which allows us to determine the probability of not exceeding specified performance goals.

III. Atmospheric Data

The influence of the atmosphere on the acoustic signature is represented in Eq. 3 by terms ρ_0, c_0 and the relaxation time parameter θ_ν. The relaxation time depends not only on local temperature and pressure, but also on the water content (relative humidity) of the air.[24,26] Furthermore, the acoustic ray path depends on temperature stratification and winds, which also affect the Blokhintzev invariant and convection during propagation.[25] All meteorological conditions are obtained from the European Centre for Medium-Range Weather Forecasts ERA5 reanalysis database.[27] The atmospheric profiles are available at 0.25° resolution in latitude and longtitude at hourly intervals.

We use a 20-year window of atmospheric observations (2003-2022) at Edwards AFB, California. Pressure, temperature, relative humidity and horizontal winds are sampled at preset isobaric values, which results in

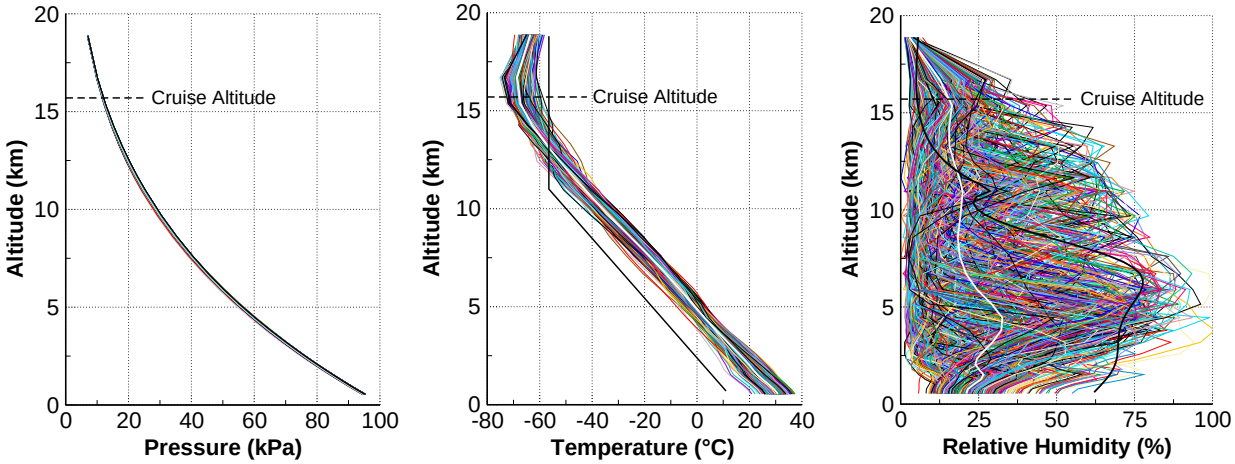


Figure 2: Atmospheric data over Edwards AFB (elevation 704 m). Each plot contains 620 profiles obtained from 2003 to 2022 during August at 10 am local time. Also shown are mean profiles (solid-white) and standard-atmosphere profiles (solid-black) for T and RH.

25 samples between the ground height at Edwards (elevation 704 m) and the cruise altitude of approximately 16 km. Since mornings are more likely times for test flights, we select 10 am local time (18:00 UTC) and pick the month of August. Selecting a particular month and time minimizes seasonal and diurnal cycles from biasing the statistics. Figure 2 shows the pressure, temperature and relative humidity data, where we plot 620 profiles corresponding to all 10 am August 2003-2022 data. The temperature and relative humidity plots also show the mean profiles (solid-white) and the standard-atmosphere profiles[a] (solid-black). The desert location of Edwards features low humidity and high summer temperatures. We assume no clouds[28] or winds, and ignore the effects of atmospheric turbulence.[29]

IV. Numerical Methods

A. Nearfield and Farfield Solvers

In the nearfield, we use the Cart3D solver.[30–33] Equation 1 is discretized on a multilevel Cartesian mesh with embedded boundaries. The mesh consists of regular Cartesian hexahedra everywhere, except for a layer of body-intersecting cells, or cut cells, adjacent to the wetted surface of the aircraft. The spatial discretization uses a cell-centered, second-order accurate finite volume method. Steady-state flow solutions are obtained using a five-stage Runge–Kutta scheme with local time-stepping, multigrid, and a domain decomposition scheme for parallel computing. All boundary conditions are enforced weakly. The implementation used in this work is Cart3D version 1.5.9.[34]

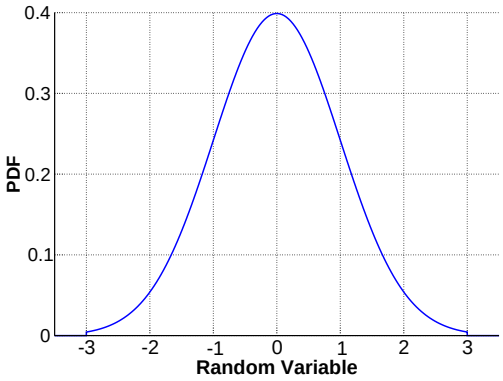
In the farfield, we solve Equation 3 using the sBOOM shock propagation solver developed by Rallabhandi[25,35] to propagate a waveform extracted from the nearfield and to compute the loudness metrics. Equation 3 is solved in the time domain using operator splitting along ray paths that account for the state of the atmosphere. The implementation used in this work is sBOOM version 2.9.1.[36] Both solvers have been thoroughly validated.[37–40]

B. Statistics

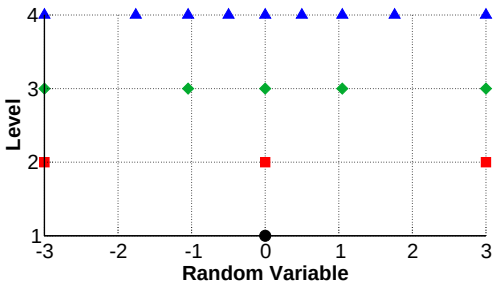
Uncertainty estimates are obtained via the QUEST software developed by Barth.[18,41–43] Equations 5 and 6 are evaluated through use of numerical integration, where the integrals are converted to a summation over N realizations of the output (simulations) corresponding to N quadrature values of the random variable ξ

$$J_H(p_H(x,\xi_1)),\ J_H(p_H(x,\xi_2)),\ \ldots,\ J_H(p_H(x,\xi_N)) \tag{9}$$

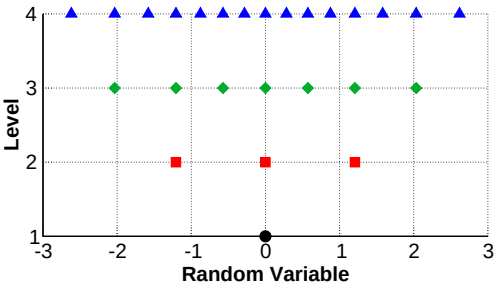
[a]Temperature from US Standard Atmosphere (1976); relative humidity from ANSI S1.26, Annex C



(a) $\xi = \mathcal{N}_{3\sigma}(\mu = 0, \sigma^2 = 1)$



(b) Clenshaw-Curtis quadrature points



(c) Gauss-Patterson quadrature points

Figure 3: Node-nested quadrature points from Clenshaw-Curtis and Gauss-Patterson formulas (right) for a normally distributed input random variable (left)

This is accomplished by first transforming Eq. 5 to a more convenient form

$$E[J] = \int J(p(x, \xi(\omega)))d\omega \tag{10}$$

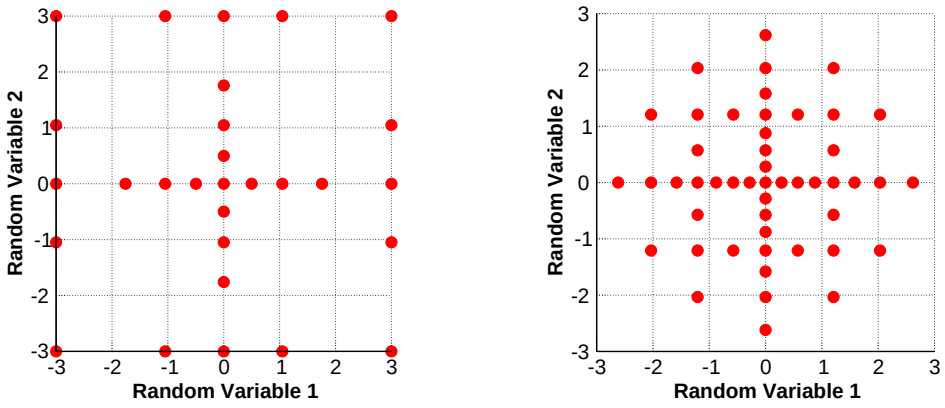
using the mapping $d\omega = f(\xi)d\xi$ and applying N-point quadrature. This results in a discrete form of Eq. 10 given by

$$E_N[J_H] = \mu = \sum_{i=1}^{N} (w\, J_H)_i \tag{11}$$

where the w values are quadrature weights. For example, if ξ is the freestream Mach number, then statistics for the loudness metrics due to variability in the input Mach number are determined from N independent simulations.

Clenshaw-Curtis[44] and Gauss-Patterson[45] formulas are used to set the quadrature points and weights. The quadratures are implemented in a hierarchical, node-nested form. The number of points N is expressed as a function the of the quadrature level L. For both quadratures, $N(L = 1) = 1$. When $L > 1$, the Clenshaw-Curtis quadrature requires $N = 2^{L-1} + 1$ points. The Gauss-Patterson quadrature requires $N = 2^L - 1$ points. Figure 3 illustrates the node nesting of both quadratures for a normally distributed random variable with zero mean and unit variance truncated at 3σ, $\xi = \mathcal{N}_{3\sigma}(\mu = 0, \sigma^2 = 1)$. In practice, $L < 3$ quadratures are too coarse. We use $L = 4$ in this work. The Gauss-Patterson quadrature is generally more accurate, but the Clenshaw-Curtis quadrature requires fewer points.

So far, the discussion considered a single random variable. A limitation of dense quadratures is that the number of quadrature points N increases exponentially with the number of random variables, D. For example, for the Clenshaw-Curtis quadrature $N = (2^{L-1} + 1)^D$. This means that for a modest problem with $D = 8$ sources of uncertainty evaluated using $L = 4$ quadrature, $N = 9^8$. This is more than 43 million points, which is not practical when a high-fidelity simulation is involved at each point. Sparse Clenshaw-Curtis and Gauss-Patterson quadratures can be used to dramatically reduce the computational cost when the problem is sufficiently smooth.[18] The number of quadrature points is proportional to $\mathcal{O}(D^{2L-1}/(2L-1)!)$. For our $(D = 8, L = 4)$ example, the number of points is reduced from 43 million to a practical 849. While the details can be found in Refs. 18 and 43, here it is sufficient to understand the sampling patterns. Figure 4 shows the quadrature point locations for a problem with two sources of uncertainty, $\xi_{1-2} = \mathcal{N}_{3\sigma}(\mu = 0, \sigma^2 = 1)$, and



(a) Clenshaw-Curtis, 29 points (b) Gauss-Patterson, 49 points

Figure 4: Sparse ($L = 4$) quadrature point locations for two random variables, $\xi_{1-2} = \mathcal{N}_{3\sigma}(\mu = 0, \sigma^2 = 1)$

$L = 4$. Along the main axis of each variable, the points are identical to those shown in Fig. 3. In contrast to the Gauss-Patterson quadrature, the Clenshaw-Curtis quadrature samples at the limits of each distribution before adding internal points.

Kernel density estimation is used to generate the probability density function p in Eq. 7. The approach is described by Barth[18,42,43] and is based on a Gaussian kernel. A response surface for J is constructed from the N quadrature points to allow draws from a large population of samples ($\gg N$) efficiently. Mean-value conditional standard-deviation fractions[43] are used to rank the input random variables based on their contribution to the standard deviation of J

$$\mathrm{R}_i = \frac{\sigma_i[J \mid \xi_{j\neq i} = \mu_{j\neq i}]}{\sigma[J]} \tag{12}$$

where the subscript i denotes the ith input random variable ξ_i and j is the set of random variables not ξ_i.

C. Karhunen-Loève (KL) Expansion

The atmospheric profiles presented in Section III can be viewed as an ensemble of random fields

$$\mathbf{w} = \{\mathbf{w}_1, \ldots, \mathbf{w}_k, \ldots, \mathbf{w}_K\} \tag{13}$$

where $\mathbf{w}_k$ represents a profile of one of the measured variables, e.g., pressure, temperature or relative humidity. Each $\mathbf{w}_k$ consists of M discrete data points in altitude, $\mathbf{w}_k \in \mathbb{R}^M$, and there are a total of K profiles in the ensemble. The data is correlated in altitude. For example, temperature fluctuations at one altitude are likely to affect the temperatures at nearby altitudes. Our goal is to construct a compact, stochastic model of the atmosphere. In other words, we seek a parametric representation of the members of $\{\mathbf{w}_k\}$ in terms of independent (uncorrelated) and identically distributed random variables suitable for integration with the quadrature methods described in Section B.

The Karhunen-Loève (KL) expansion[16–18] is an optimal compression technique for Gaussian process correlated random fields. The expansion is traditionally applied to continuous fields. Since the atmospheric data is sampled at discrete intervals, we use a discrete analogue of the KL expansion, frequently called principal component analysis. Each profile is modeled in the following form

$$\widetilde{\mathbf{w}}_k = \boldsymbol{\mu}(\mathbf{w}) + \mathbf{w}'_k = \boldsymbol{\mu}(\mathbf{w}) + \sum_{i=1}^{M} \xi_i(\omega)\sqrt{\lambda_i}\boldsymbol{\phi}_i \tag{14}$$

where $\boldsymbol{\mu}(\mathbf{w})$ is the mean profile of the measured ensemble, $\mathbf{w}'_k$ is a perturbation and $\lambda_i, \boldsymbol{\phi}_i$ are eigenpairs associated with the sample covariance matrix

$$\mathbf{C} = \frac{1}{K-1}\mathbf{W}\mathbf{W}^{\mathrm{T}} \tag{15}$$

The matrix $\mathbf{W}$ is formed from the data by subtracting the mean

$$\mathbf{W} = [\mathbf{w}_1 - \boldsymbol{\mu}(\mathbf{w}), \ldots, \mathbf{w}_K - \boldsymbol{\mu}(\mathbf{w})] \tag{16}$$

The parameters $\xi_i(\omega)$ in Eq. 14 are the independent random variables that parameterize the ensemble. Each variable is normally distributed with zero mean and unit variance, $\xi_{1-M} = \mathcal{N}(\mu = 0, \sigma^2 = 1)$. The random process is completely parameterized by the M eigenpairs and the associated ξ_M random variables.

To compress the parameterization, we truncate the KL expansion. Note that $\mathbf{C}$ is symmetric with M real and non-negative eigenvalues. The eigenvalues are sorted in descending order

$$\lambda_1 \geq \lambda_2 \geq \cdots \geq \lambda_m \geq \cdots \geq \lambda_M \tag{17}$$

where λ_1 is the largest eigenvalue of $\mathbf{C}$. The sum in Eq. 14 is truncated after $m < M$ terms corresponding to the m largest eigenvalues, indicated by KLm notation. Choosing m is guided by recognizing that the total variance of the ensemble is given by

$$V[\mathbf{w}'] = E\left[(\mathbf{w}')^2\right] = \sum_{i=1}^{M} \lambda_i \tag{18}$$

and defining the cumulative variance ratio based on the variance of the truncated expansion

$$V_{\mathrm{CR}} = \frac{\sum_{i=1}^{m} \lambda_i}{\sum_{i=1}^{M} \lambda_i} \tag{19}$$

Setting m so that V_{CR} is above a user-specified threshold ensures that the total variance of the truncated expansion is sufficiently close to the variance of the measurements. Additional criteria, e.g., local maximum error tolerances, are usually required to check that the distribution of variance along the mean profile is acceptable.

V. Results

A. Stochastic Model of the Atmosphere for Edwards AFB

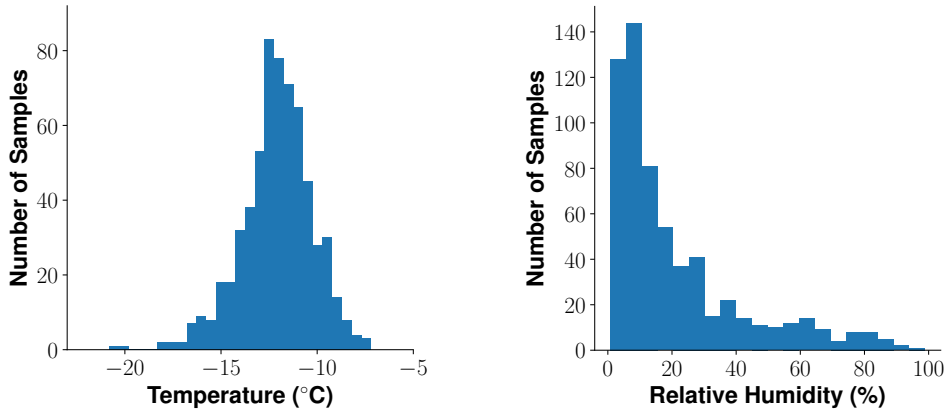


Figure 5: Histograms from measured temperature (left) and relative humidity (right) data at 6.7 km altitude

We begin by assessing the atmospheric data shown in Fig. 2 for KL representation. Recall that KL expansions presume a Gaussian process that is not bound by strict intervals. Figure 5 shows histograms of temperature and relative humidity from an altitude of 6.7 km. These histograms are representative of data at other altitudes as well. The temperature data is unconstrained and the histogram is essentially Gaussian. In contrast, relative humidity is strongly skewed to the right, resembling a beta distribution. Furthermore, relative humidity is bounded between 0 and 100%. While KL expansions for non-Gaussian and interval data exist, we explore a variable transformation approach well known in aviation that offers several advantages.

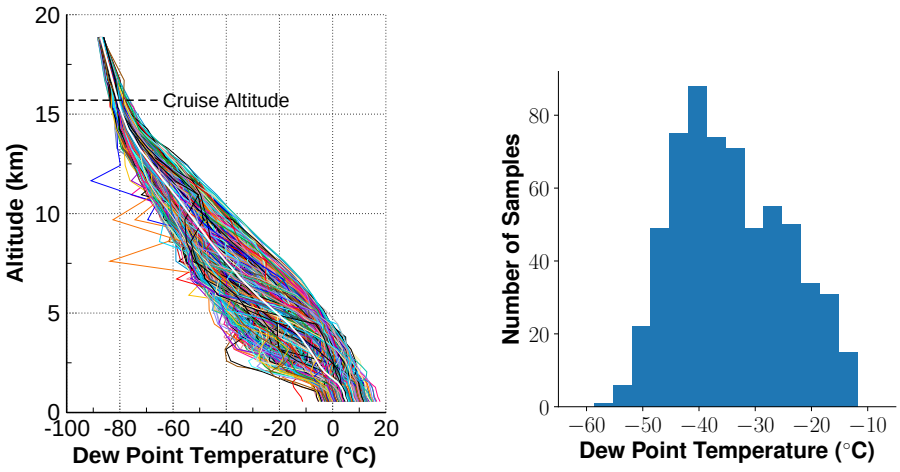


Figure 6: T_d profiles (left) and histogram extracted at 6.7 km altitude (right)

Relative humidity, RH, is closely related to dew point temperature, T_d, which in turn depends on ambient temperature, T. To transform relative humidity to dew point temperature, we start with a definition of relative humidity[46]

$$RH = 100\frac{p_e}{p_s} \tag{20}$$

where p_e is the equilibrium water vapor pressure and p_s is the saturation water vapor pressure. An empirical equation is used to express the saturation vapor pressure as a function of temperature[46]

$$p_s = 6.1121\mathrm{e}^{\frac{17.62T}{243.12+T}} \tag{21}$$

where T is in °C and p_s in hPa. Substituting Eq. 21 into Eq. 20 and using the definition for dew point temperature T_d

$$p_e = p_s(T_d) \tag{22}$$

we obtain the following expression for dew point temperature

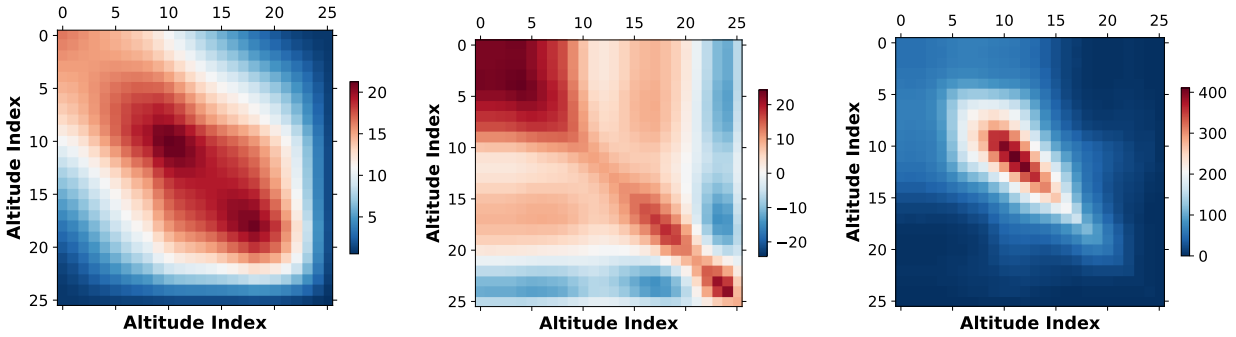
$$T_d = \frac{243.12\left(\ln\left(\frac{RH}{100}\right) + \frac{17.62T}{243.12+T}\right)}{17.62 - \ln\left(\frac{RH}{100}\right) - \frac{17.62T}{243.12+T}} \tag{23}$$

Figure 6 shows the dew point temperature profiles obtained from the measured T and RH values using Eq. 23. The distribution appears centered about its mean (solid-white) and the bounds on relative humidity have been sidestepped. Figure 6 also shows a histogram of dew point temperature extracted at 6.7 km, which is at the same altitude as the histograms in Fig. 5. Transforming RH to T_d transforms the shape of the histogram close to a normal distribution. These factors make T_d a much better candidate for KL expansion.

Referring to Eqs. 13 and 15, each profile $\mathbf{w}$ consists of 26 data points in altitude and there are 620 profiles in the dataset for each variable, i.e., $K = 620$ and $M = 26$. Figure 7 shows the values of the covariance matrices for pressure, temperature and dew point temperature, revealing the expected altitude correlation (larger altitude index indicates higher altitude). The largest values are near the diagonal, indicating a strong association with nearby data. Figure 8 shows the eigenvalues, sorted by magnitude, of each covariance matrix. The eigenvalues span orders of magnitude. The pressure eigenvalues (black circles) decay the fastest. Temperature (red squares) and dew point temperature (green triangles) eigenvalues have similar decay rates and the dew point temperature eigenvalues are the largest in magnitude.

The similar eigenvalue decay for the temperature variables and the direct relationship between T, T_d and RH in Eq. 23 suggests a combined KL expansion that captures the interdependence of these variables. We redefine the ensemble vector $\mathbf{w}$ as a composite of the two temperatures

$$\mathbf{w} = \begin{bmatrix} \mathbf{T} \\ \mathbf{T_d} \end{bmatrix} \tag{24}$$



(a) Pressure (b) Temperature (c) Dew point temperature

Figure 7: Covariance matrices from Edwards atmospheric data

and proceed with the KL expansion. Once we obtain the covariance eigenpairs, we separate the temperatures and use the inverse of Eq. 23 to solve for RH from the modeled T and T_d pairs.

Figure 9 shows the covariance matrix and eigenvalues for the (T, T_d) system. The covariance matrix is twice the size ($M = 52$) of the single variable matrix. The left plot of Fig. 9 shows the largest covariance values in the lower diagonal block corresponding to dew point temperature (identical to Fig. 7c). The off-diagonal blocks highlight the interdependence of the two temperatures. The center plot of Fig. 9 shows that the largest eigenvalues (blue circles) closely follow the eigenvalues of dew point temperature. The right plot of Fig. 9 shows the relationship between the cumulative variance ratio, Eq. 19, and the ordered eigenvalues.

We now consider a truncated KL expansion of the combined (T, T_d) system to construct a compact model of the atmosphere. The center plot of Fig. 9 shows that the six largest eigenvalues form a group which exceeds a value of 100 and spans a factor of 30. The right plot of Figure 9 shows that these six eigenvalues capture more than 90% of the total variance. Hence, we begin by truncating the KL series after six terms, i.e., $m = 6$ is selected in Eqs. 14 and 17.

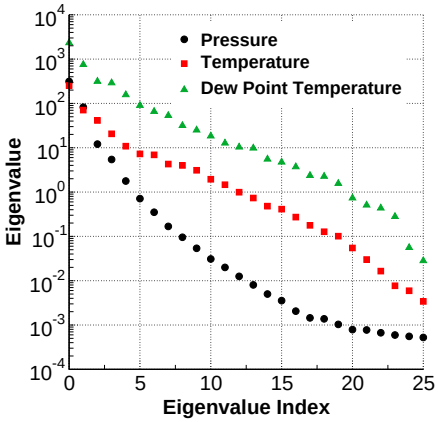


Figure 8: Covariance eigenvalues

Associated with the eigenvalues are six normally distributed random variables $\xi_{1-6} = \mathcal{N}_{3\sigma}(\mu = 0, \sigma^2 = 1)$, e.g., recall Fig. 3a. We limit the normal distribution to 3σ to avoid extreme atmospheric conditions. We assess both the Clenshaw-Curtis and Gauss-Patterson sparse ($L = 4$) quadratures for estimating the moment statistics.

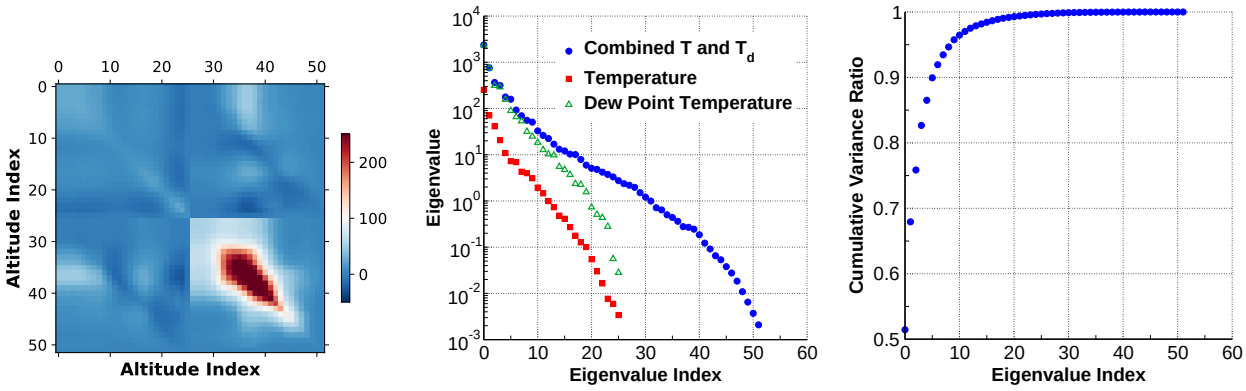
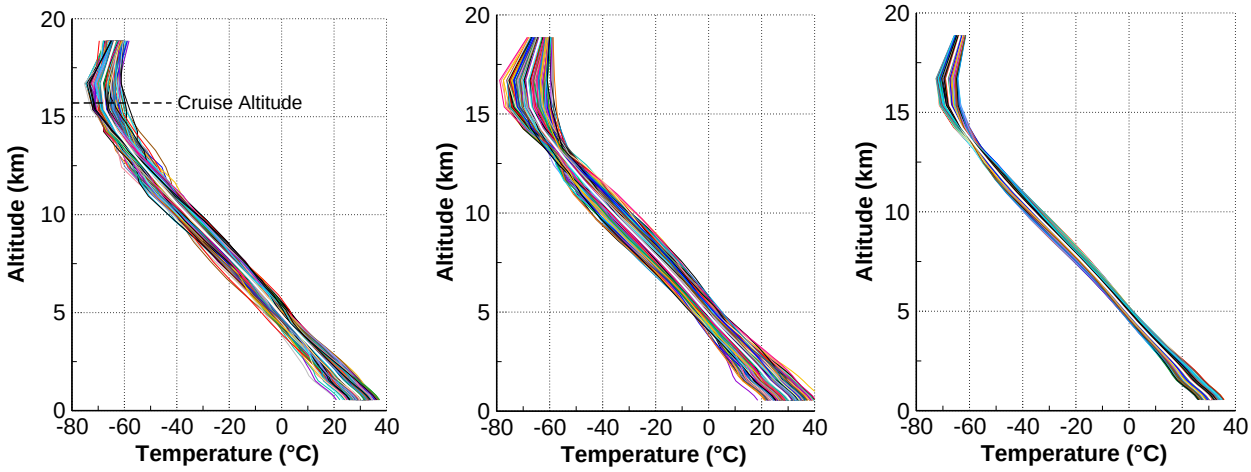
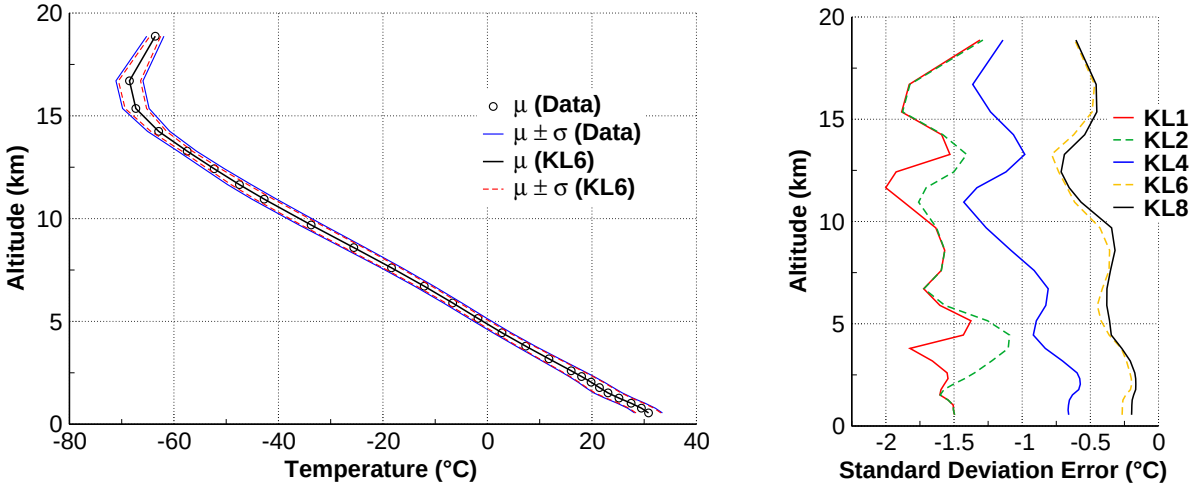


Figure 9: Covariance matrix (left), eigenvalues (center) and cumulative variance ratio (right) of the combined (T, T_d) system. The eigenvalues of T and T_d, reproduced from Fig. 8, are included for reference.



(a) Measured data (620 profiles) (b) Clenshaw-Curtis (389 profiles) (c) Gauss-Patterson (545 profiles)

Figure 10: Comparison of measured temperature profiles (left) with profiles obtained using KL6 expansion

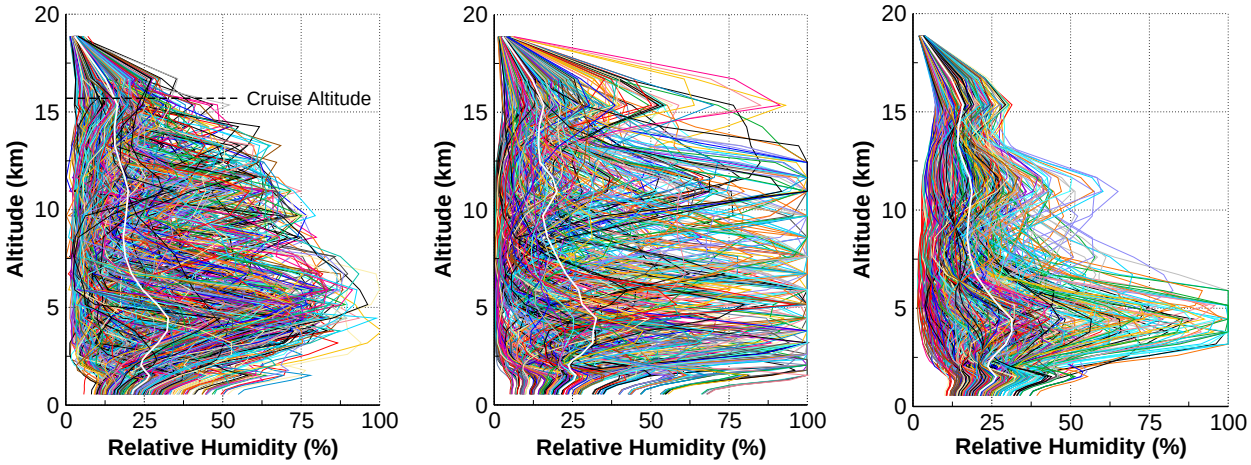


(a) Measured data and KL6 expansion (b) Error relative to measured data

Figure 11: Comparison of mean (μ) and standard deviation (σ) temperature statistics between measured data and truncated KL expansions using the Gauss-Patterson quadrature

Figure 10 compares the temperature profiles of the measured dataset with those obtained using the KL6 expansion. The ensemble generated using the Clenshaw-Curtis quadrature contains 389 profiles. The Gauss-Patterson quadrature contains 545 profiles. The sample profiles obtained using the Clenshaw-Curtis quadrature in Fig. 10b show larger spread, modeling some of the rarer profiles observed in the measured data. This is because the Clenshaw-Curtis quadrature samples the 3σ limit of the random variables, as illustrated in Fig. 4a. The Gauss-Patterson quadrature samples closer to the mean of the normal distribution, which results in a tighter distribution of temperature profiles shown in Fig. 10c. Despite the different sampling patterns, the Clenshaw-Curtis and Gauss-Patterson quadratures predict very similar moment statistics. This is because the samples at the 3σ limit are assigned small weights when evaluating the statistics via Eq. 11.

To examine the accuracy of the moment statistics, Fig. 11 compares the mean (μ) and standard deviation (σ) of the measured profiles with those of the KL6 expansion evaluated using the Gauss-Patterson quadrature. Figure 11a shows excellent agreement in the μ and σ statistics. The agreement in the mean is expected for any KL expansion because $\mathbf{w}'$ in Eq. 14 is a zero-mean process. Figure 11a also shows that the errors in σ are small throughout the profile, with slight differences visible at higher altitudes. In Fig. 11b, we isolate the errors in σ and examine the sensitivity of the expansion to the number of terms m. The error is computed relative to the standard deviation of the measured data and negative error means that the standard deviation



(a) Measured data (620 profiles) (b) Clenshaw-Curtis (389 profiles) (c) Gauss-Patterson (545 profiles)

Figure 12: Comparison of measured RH profiles (left) with profiles obtained using KL6 expansion

of the KLm expansion underestimates the standard deviation of the measurements, as expected from Eq. 19. Figure 11b shows that the errors decrease as more terms are added. The error is close to 2°C at upper altitudes for the KL1 expansion (red line). This error is reduced to about 0.25°C at lower altitudes with the KL6 expansion and increasing to KL8 (black line) does not reduce the errors significantly.

Figure 12 compares the relative humidity profiles of the measured dataset with those obtained using the KL6 expansion. The difference in the character of the ensembles is striking, especially for the Clenshaw-Curtis quadrature shown in Fig. 12b. Recall that the eigenpairs are computed for the (T, T_d) system, and RH is obtained from the stochastic T and T_d profiles via Eq. 23. Equation 20 implies a $T_d \leq T$ constraint, otherwise the air is saturated with moisture indicating the onset of precipitation. This means that in some profiles, T_d may locally exceed T. When this occurs, we force $T_d = T$ at that particular altitude, which results in relative humidity of 100%. The limiting is more frequent in the Clenshaw-Curtis ensemble because it samples the 3σ bounds of the random variables. The Gauss-Patterson quadrature generates profiles in better agreement with the observed profiles.

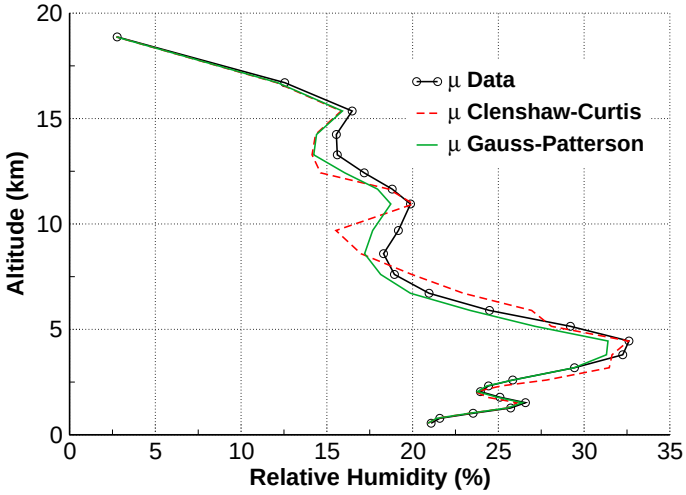


Figure 13: Comparison of relative humidity mean (μ) between measured data and KL6 expansions

Figure 13 compares the mean of the measured RH ensemble with those obtained via the Clenshaw-Curtis and Gauss-Patterson quadratures (originally solid-white lines in Fig. 12). Unlike temperature, agreement in the mean is not guaranteed because RH is obtained from the (T, T_d) system. The mean of the Gauss-Patterson ensemble (solid-green) has a smoother profile and is in closer agreement with the observed mean

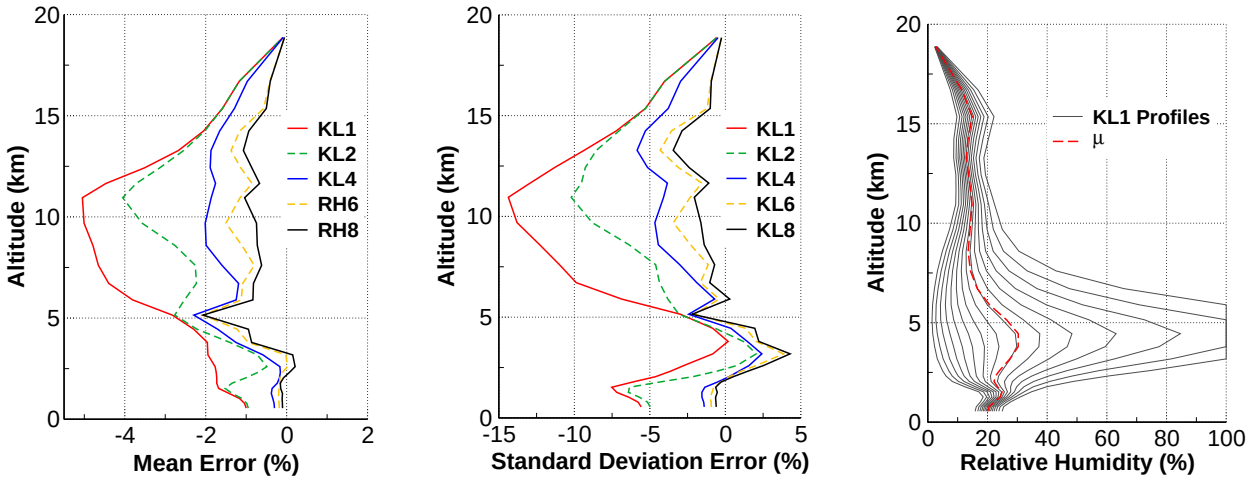


Figure 14: Comparison of errors in the mean (left) and standard deviation (center) for relative humidity relative to measured data. Profiles of the KL1 expansion (right) explain the large KL1 errors near 10 km.

(black-circles), especially at lower altitudes. Figure 14 shows a detailed examination of the errors in the moment statistics for a sequence of KL expansions. The errors are evaluated relative to the statistics of the measured data. We present results for the Gauss-Patterson quadrature because we find that for $L = 4$ quadrature it has smaller errors and less erratic error distributions. Negative errors in Fig. 14 indicate that the KL expansion underestimates the measurements. For highly truncated expansions, such as KL1, the errors in the mean and standard deviation are large. To explain this, the right plot of Fig. 14 shows the relative humidity profiles for the KL1 expansion. We observe that the spread in the KL1 profiles is too small compared to the measured profiles shown in Fig. 12a near the 10 km mark, which leads to the large errors. KL4 expansion (solid-blue) begins to model this region well and there is only a small reduction in errors between the KL6 and KL8 expansions.

Overall, the KL6 expansion based on the (T, T_d) system strikes a pragmatic compromise between model accuracy and low-dimensional representation. The cumulative variance ratio in Fig. 9 suggests that a KL10 expansion might be appropriate if high accuracy is desired. Conversely, if maximum compression of the stochastic process has priority, then the results show that the KL4 expansion captures the standard deviation of T profiles within 1.5°C and has less than 2% error in the mean and 5% error in the standard deviation of RH profiles. The KL6 expansion reduces these errors by a factor of two with just two additional variables.

B. X-59 Loudness Analysis

Having established the fidelity of the KL expansion for atmospheric uncertainty, we examine the impact of this uncertainty on acoustic signatures of the X-59 aircraft. The aircraft geometry used in the simulations is the "C612A" model of the X-59. Figure 15 shows the airframe, control surfaces, engine inlet and nozzle, and near-body flow solution at nominal cruise conditions, $M_\infty = 1.4$ and $\alpha = 2.09°$. The model includes three outflow boundaries to model inlets and five inflow boundaries to model exhaust nozzles. The aircraft geometry also includes vortex generators and various probes. The permeable boundary conditions and geometric details are all necessary to resolve the pressure signatures accurately.

1. Uncertain Atmosphere

The KL6 expansion is used to model the randomness of the temperature and relative humidity profiles. Recall from Eq. 14 that this expansion is parameterized with six normally distributed input random variables with zero mean and unit variance $\xi_{1-6} = \mathcal{N}_{3\sigma}(\mu = 0, \sigma^2 = 1)$. The moment statistics, Eqs. 5 and 6, of the ground pressure signature and noise metrics are evaluated with the same sparse Gauss-Patterson ($L = 4$) quadrature as used in Section A. This generates 545 temperature and relative humidity profiles, shown in Figs. 10c and 12c, respectively, that define the state of the atmosphere for propagating the pressure signature from the aircraft to the ground.

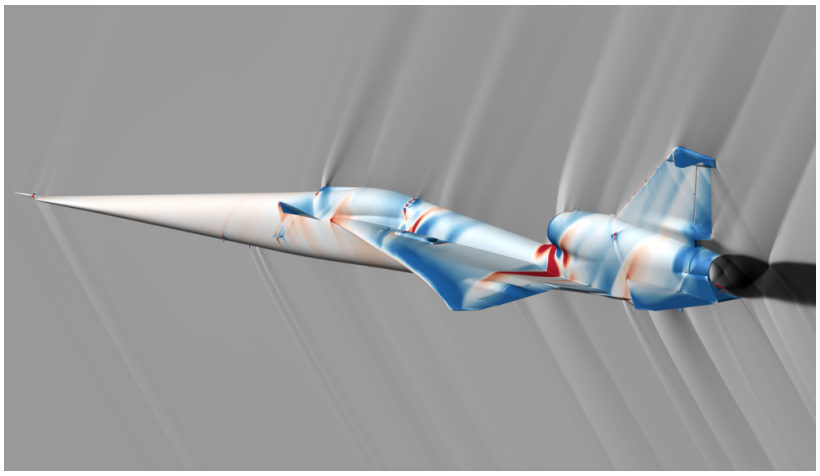


Figure 15: X-59 geometry and near-body flow at nominal conditions, $M_\infty = 1.4$ and $\alpha = 2.09°$. Aircraft surface is colored by C_p (red denotes pressures above freestream, blue below). Gray scale is used to visualize shocks via density variations on a plane through the aircraft's centerline.

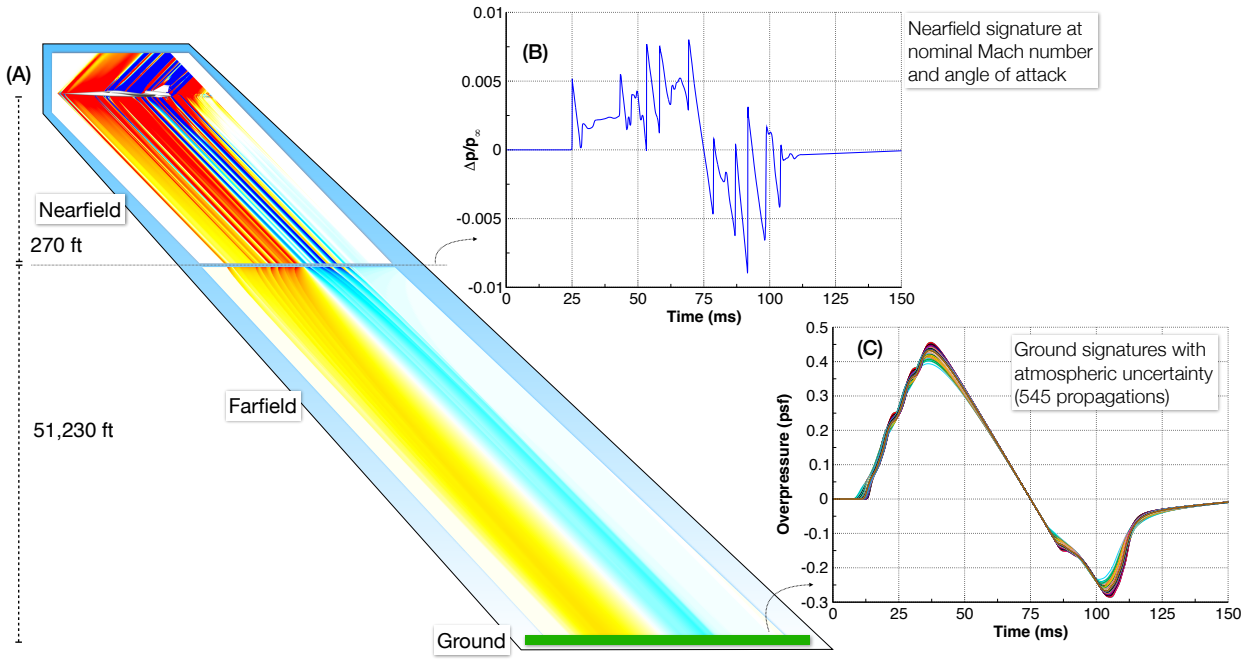


Figure 16: Overview of computational domain (A) showing pressure contours on a plane through the aircraft's centerline (red indicates pressures above ambient, blue below). The nearfield and farfield domains are not drawn to scale. Frame B shows the nominal nearfield signature. Frame C shows each realization of the ground signature due to atmospheric uncertainty in the farfield domain.

Figure 16 provides an overview of the simulations. On the left side, frame A shows the pressure contours in the nearfield and farfield domains. The domains interface via a nearfield pressure signature, Eq. 4. This signature is extracted at a distance of 270 ft (three body lengths) from the aircraft. Note that the two domains are not drawn to scale, the farfield is vastly larger. Frame B shows the nearfield signature at nominal cruise conditions. The signature contains many shocks that can be seen originating from the various geometric features of the aircraft (see Fig. 15). To isolate the effects of the atmospheric uncertainty, we initially assume no uncertainty in the nearfield, i.e., the flights conditions are fixed at their nominal values and there is no randomness in the nearfield signature. The atmospheric uncertainty is imposed in the farfield domain. The signature is propagated through the 545 temperature and relative humidity profiles to obtain the ground signatures shown in Frame C. We use a sampling frequency of 100 kHz. The variability in the waveforms directly reflects the influence of the atmospheric conditions.

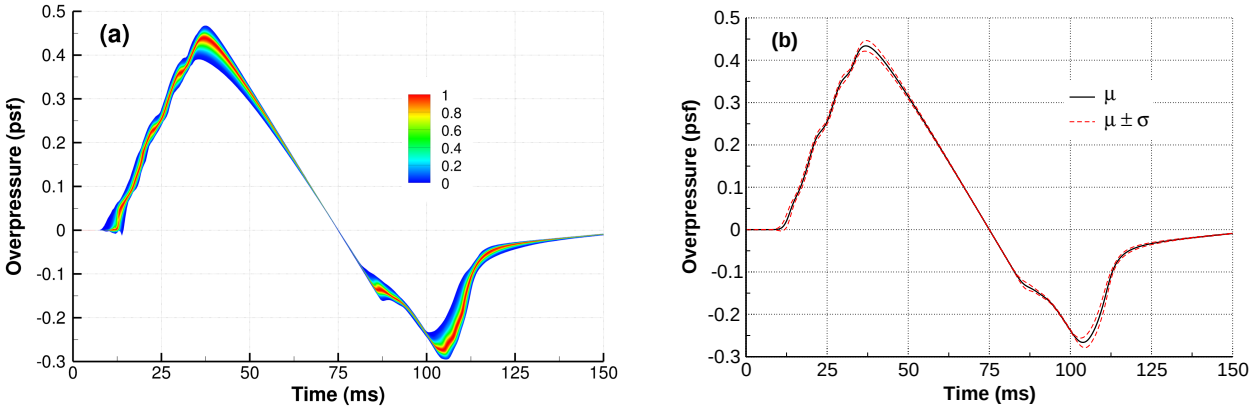


Figure 17: Probability density function of the ground signature with contour cut-off set at 0.05% (left) and the mean signature ($\boldsymbol{\mu}$) with standard deviation ($\boldsymbol{\sigma}$) envelope (right)

Figure 17a shows the probability density function, p in Eq. 7, of the ground waveform to fully characterize the uncertainty in the signature due to uncertainty in the atmosphere, specifically randomness in T and RH profiles. As expected, the largest uncertainties are in amplitude and duration. The zero crossing of the signature shows no variability because in the reference frame of the wave it remains fixed, as indicated in the farfield pressure contours of Fig. 16. Note that at any time value in Fig. 17a, the cross section of p appears Gaussian. This implies that the mean and standard deviation statistics should accurately characterize the uncertainty in the pressure signature.[10] Figure 17b shows the mean signature $\boldsymbol{\mu}$ and the $1\boldsymbol{\sigma}$ envelope. The envelope is fairly close to the mean, with largest values at the peaks and at the foot of the positive amplitude wave. The $\boldsymbol{\mu}$ and $\boldsymbol{\sigma}$ statistics are in good agreement with the probability density function.

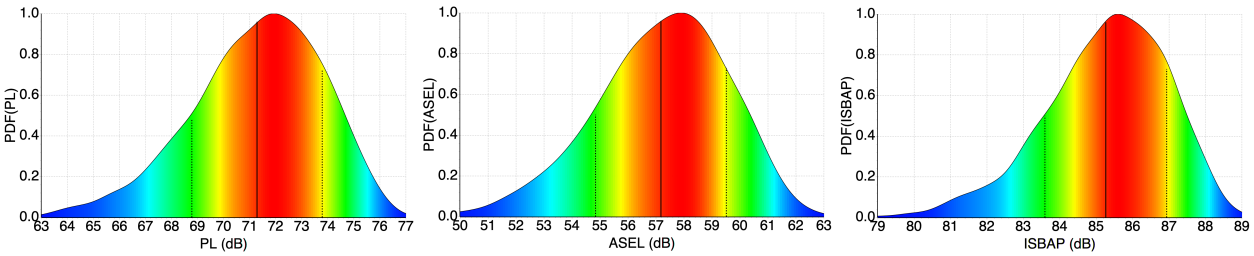
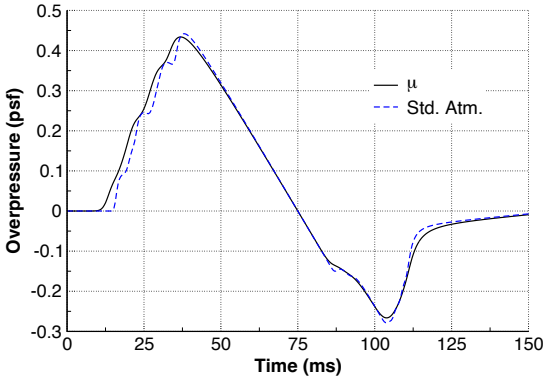


Figure 18: Probability densities of PL (left), ASEL (center) and ISBAP (right) for propagation with atmospheric uncertainty. Mean (solid line) and standard deviation (dashed) are also shown.

Figure 18 shows the estimated probability density functions of three selected noise metrics: PL (left), ASEL (center) and ISBAP (right). The superimposed lines indicate the mean and standard deviation of each metric. The probability densities are unimodal with mild skewness to the left, which could be explained by the skewness in the measured RH profiles. Similar distributions are also estimated by Lazzara *et al.*[6] and Doebler *et al.*[5] The mean and standard deviation characterize the distributions well. We obtain the following noise values: PL= 71.3 ± 2.5 dB, ASEL= 57.2 ± 2.3 dB and ISBAP= 85.3 ± 1.7 dB. Despite the seemingly small uncertainty in the ground signature observed in Fig. 17b, the atmospheric fluctuations cause a moderate uncertainty of 4 to 8% in the noise metrics.



	Std. Atm.	μ
PL (dB)	77.3	71.3
ASEL (dB)	63.2	57.2
ISBAP (dB)	89.0	85.3

Figure 19: Comparison of mean signature and noise metrics with atmospheric uncertainty expected at Edwards (μ) to those obtained using propagation in standard atmosphere (Std. Atm.)

To highlight the importance of including a realistic atmosphere in noise predictions, Fig. 19 compares the mean signature with the atmospheric uncertainty expected at Edwards to a signature propagated through the standard atmosphere. The standard-atmosphere profiles used in this work are shown in Fig. 2. The signature resulting from propagation through the standard atmosphere shows less attenuation of the leading shocks, which is primarily due to the higher relative humidity at altitudes below 10 km. Moreover, the total duration of the signature is shorter with a steeper recompression (near 110 ms), which suggests a louder waveform. This is confirmed in the table accompanying Fig. 19 that lists the metric means presented in Fig.18 and those obtained in the standard atmosphere. The table shows that there are significant increases in loudness; for example, PL is 5 dB higher in the standard atmosphere. This is beyond the 2σ envelope in Fig.18, which means that loudness values from the standard atmosphere are not representative of test flights at Edwards. We observe similar trends in ASEL and ISBAP, and our estimates are in good agreement with published results.[5,6]

2. *Combined Nearfield and Atmospheric Uncertainty*

For the final test case, we introduce uncertainty in the nearfield domain in addition to uncertainty in the state of the atmosphere. We consider the cruise Mach number, $M_\infty = \mathcal{N}_{3\sigma}(\mu = 1.4, \sigma = 0.0066)$, and altitude, $A_c = \mathcal{N}_{3\sigma}(\mu = 51,500 \text{ ft}, \sigma = 500)$ as uncertain. Together with the KL6 expansion, this gives a total of eight input random variables. The sparse Gauss-Patterson ($L = 4$) quadrature requires 1,121 simulations to estimate the moment statistics, which is roughly a twofold increase over the six variable case.

Before presenting the statistics, we briefly address computational cost. The turn-around of a farfield solution is several minutes on a single core of a laptop computer. In contrast, a single X-59 nearfield simulation requires approximately five wall-clock hours on an engineering workstation. It is important to realize that the structure of the problem allows a separation of variables approach.[10] In particular, the atmospheric uncertainty does not affect the nearfield simulations, e.g. the previous test case required only a single nearfield simulation at nominal conditions. For problems with uncertainty sources in both domains, the tensor-product form of sparse quadratures allows us to precompute unique nearfield simulations that we use in the evaluation of the farfield uncertainty without any loss in accuracy of the output statistics. For the current case of 1,121 simulations, there are only 15 unique nearfield solutions.

Figure 20a shows the 15 nearfield signatures that account for uncertainty in M_∞. We center the waveforms on the zero crossing of the main expansion. The uncertainty in M_∞ causes variability in shock strengths, and subtle changes in shock positions and signal duration. Figure 20b shows the 1,121 ground signatures resulting from propagation of the nearfield signatures from an uncertain altitude and through an uncertain atmosphere. The dispersion in the ground signatures due to the additional uncertainties is slightly larger than that shown in Fig. 16 for atmospheric uncertainty only.

Figure 21a shows the probability density function and mean (solid line) due to uncertainty in M_∞, altitude and the atmosphere for PL. Superimposed (dashed-line) is the probability density function and mean due to atmospheric uncertainty only, reproduced from Fig. 18. The additional uncertainties shift the distribution to the right, increasing the value of the mean PL by 0.4 dB. The standard deviation increased slightly from

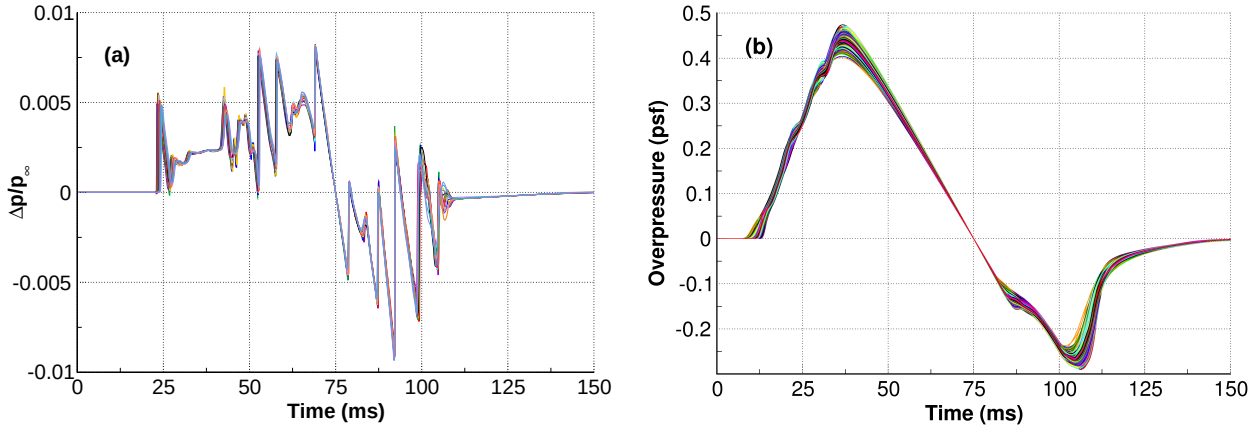
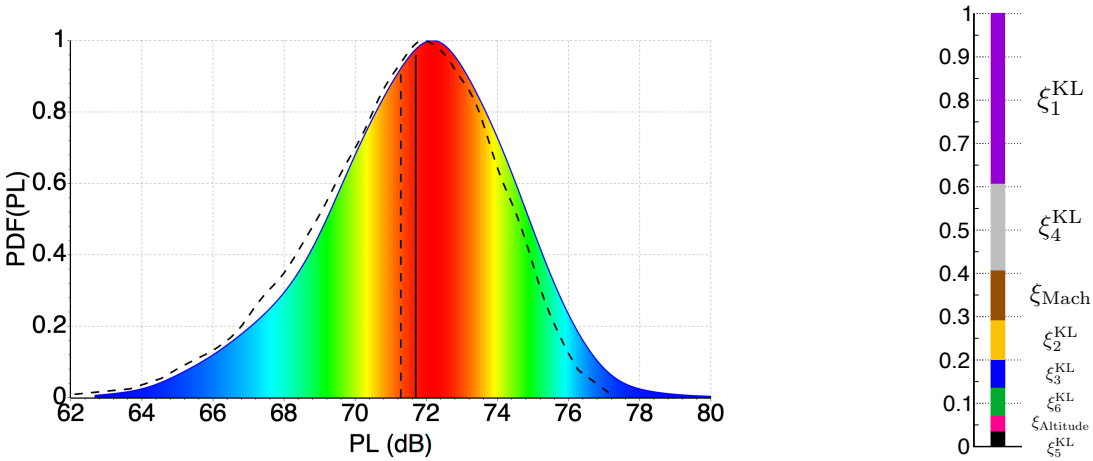


Figure 20: Nearfield signatures (left) due to uncertainty in Mach number (15 CFD simulations) and ground signatures (right) due to uncertainty in Mach number, altitude and atmosphere (1,121 farfield propagations).



(a) Probability density and mean (solid line) due to all sources of uncertainty. Superimposed (dashed) is atmospheric uncertainty only.

(b) Ranking of random variables on their fractional contribution to standard deviation

Figure 21: Uncertainty quantification for PL noise metric with ranking of sources of uncertainty

2.5 dB to 2.52 dB, indicating that the atmosphere is the primary source of uncertainty in this problem. We see similar trends with ASEL and ISBAP. Figure 21b confirms the dominance of atmospheric uncertainty. The input random variables are ranked based on their fractional contribution to the standard deviation of PL using Eq.12. Figure 21b shows that the random variables associated with the first and fourth terms of the KL expansion, ξ_1^{KL} and ξ_4^{KL}, respectively, have the largest influence on σ. It is not clear why the fourth KL term has greater influence than the second and third terms, but this could be related to the large errors shown in Fig. 14 for highly truncated KL expansions. It is not until the fourth term that uncertainty in RH at higher altitudes is modeled accurately.

Figure 22 shows the cumulative distribution function. PL values above 79 dB and below 65 dB have very low probabilities during morning test flights on any day in August at Edwards AFB. The dashed line indicates a PL value of 75 dB, which is the target limit value of PL for the X-59. The probability of observing PL below 75 dB is about 92%. This is very encouraging for the upcoming X-59 test flights; however, our estimate is based on a fixed aircraft weight and shape, and neglects the effects of trim and atmospheric turbulence.

VI. Conclusions

The Karhunen-Loève expansion provides an accurate and compact parameterization of atmospheric uncertainty in the context of noise predictions for supersonic flight. By transforming relative humidity

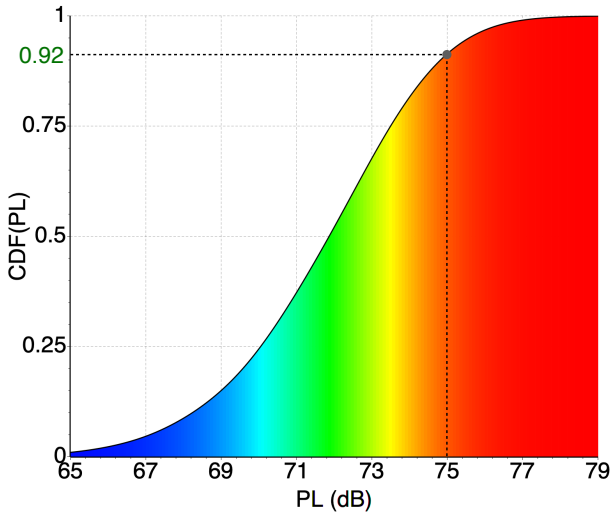


Figure 22: Cumulative distribution for PL due to uncertainty in Mach number, altitude and atmosphere

to dew point temperature, the accuracy and efficiency of the expansion is significantly improved. This variable transformation augments the covariance matrix with the interdependence of relative humidity on temperature and dew point temperature, circumvents relative humidity bounds and centers the distribution. A six-parameter stochastic model evaluated with sparse quadrature estimates the mean and standard deviation of a 20-year window of atmospheric observations over Edwards AFB to within 1% and 2.5%, respectively, for relative humidity, and provides even better agreement in temperature statistics.

The results show that the atmosphere has a major influence on the noise metrics of the X-59. Noise predictions based on the standard atmosphere are 4 to 7% louder for the PL, ASEL and ISBAP metrics compared to those obtained from the expected conditions at Edwards. Furthermore, the uncertain atmosphere causes 4-8% dispersions in terms of standard deviation. By considering additional sources of uncertainty, namely the cruise Mach number and altitude, we show that the atmosphere is the primary source of uncertainty. The first and fourth terms of the KL expansion account for approximately 60% of the standard deviation, while the cruise Mach number and altitude contribute less than 20%. The final example demonstrates that morning flights of the X-59 on any day in August have a 92% probability of not exceeding the 75 dB limit.

Overall, the KL model of the atmosphere is well suited for use with high-fidelity simulations. When combined with sparse quadratures, we achieve overnight turn-around of uncertainty quantification for loudness metrics under conditions expected during X-59 test flights on small to midsize computing clusters. This affordability is a promising step toward developing capabilities for future en route noise certification by simulation-based analysis. Future work plans include investigating better ways to incorporate dew point temperature constraints into the KL expansion, and considering additional sources of uncertainty, such as aircraft weight and winds, and accounting for aircraft trim.

Acknowledgements

The authors gratefully acknowledge support from the NASA ARMD Commercial Supersonic Technology Project. Resources supporting this work were provided by the NASA High-End Computing (HEC) Program through the NASA Advanced Supercomputing (NAS) Division at Ames Research Center. Garo Bedonian was supported by the NASA-OSTEM Internship Program. The authors thank Tim Barth for discussions on the KL expansion and development of the QUEST UQ package. The authors also thank Will Doebler (LaRC) for the Edwards data, Laura White (LaRC) for dew-point discussions, and Sriram Rallabhandi (ARC) for updates to the sBOOM code used in this work.

References

[1]Maglieri, D. J., Bobbitt, P. J., Plotkin, K. J., Shepherd, K. P., Coen, P. G., and Richwine, D. M., "Sonic Boom: Six Decades of Research," NASA/SP-2014-622, 2014, http://hdl.handle.net/2060/20150006843.

[2]West, T. K., Reuter, B. W., Walker, E. L., Kleb, B., and Park, M. A., "Uncertainty Quantification and Certification Prediction of Low-Boom Supersonic Aircraft Configurations," *Journal of Aircraft*, Vol. 54, No. 1, 2017, pp. 40–53. doi:10.2514/1.C033907, https://doi.org/10.2514/1.C033907.

[3]Phillips, B. D. and West, T. K., "Trim Flight Conditions for a Low-Boom Aircraft Design Under Uncertainty," *Journal of Aircraft*, Vol. 56, No. 1, 2019, pp. 53–67. doi:10.2514/1.C034932.

[4]Eggert, C. A., White, L., Schmidt, J. N., Phillips, B. D., and Windous, Z. D., *Method for System-Level Multidisciplinary Uncertainty Analysis of Low-Boom Flight Vehicles*. doi:10.2514/6.2024-1876.

[5]Doebler, W. J., Wilson, S. R., Loubeau, A., and Sparrow, V. W., "Simulation and Regression Modeling of NASA's X-59 Low-Boom Carpets Across America," *Journal of Aircraft*, Vol. 60, No. 2, 2023, pp. 509–520. doi:10.2514/1.C036876.

[6]Lazzara, D. S., Magee, T., Shen, H., and Mabe, J. H., *Sonic Boom Performance of Low-Boom Aircraft in Non-Standard Atmospheres*. doi:10.2514/6.2020-0792.

[7]Malbéqui, P., Normand, P.-E., Budin, L., and Carrier, G., "Sensitivity analysis of the Propagation of the Low Sonic Boom to the Aerology," e-Forum Acusticum, hal-03229481, Dec. 2020. doi:10.48465/fa.2020.0429.

[8]Blumrich, R., Coulouvrat, F., and Heimann, D., "Meteorologically induced variability of sonic-boom characteristics of supersonic aircraft in cruising flight," *The Journal of the Acoustical Society of America*, Vol. 118, No. 2, 08 2005, pp. 707–722. doi:10.1121/1.1953208.

[9]Loubeau, A. and Page, J., "Human Perception of Sonic Booms from Supersonic Aircraft," *Acoustics Today*, , No. 14, 2018, pp. 23–30.

[10]Nemec, M., Aftosmis, M. J., and Smith, L., "Uncertainty Estimates for Sonic-Boom Pressure Signatures and Loudness Carpets," AIAA Paper 2021-2753, June 2021. doi:10.2514/6.2021-2753.

[11]Doebler, W. J. and Loubeau, A., "Estimating the noise dose range of the NASA X-59 aircraft in supersonic cruise using PCBoom propagation simulations," *JASA Express Letters*, Vol. 3, No. 5, 05 2023, pp. 053601. doi:10.1121/10.0019501.

[12]Rallabhandi, S. K., West, T. K., and Nielsen, E. J., "Uncertainty Analysis and Robust Design of Low-Boom Concepts Using Atmospheric Adjoints," *Journal of Aircraft*, Vol. 54, No. 3, 2017, pp. 902–917. doi:10.2514/1.C033908.

[13]Rallabhandi, S. K. and Loubeau, A., "Summary of Propagation Cases of the Third AIAA Sonic Boom Prediction Workshop," *Journal of Aircraft*, Vol. 0, Article in Advance, pp. 1–17. doi:10.2514/1.C036327.

[14]Hutchinson, A. D. and Bowersox, R. D., "A Sonic Boom Propagation Code for Studying Atmospheric Effects and Uncertainties," AIAA Paper 2021-0010, Jan. 2021. doi:10.2514/6.2021-0010.

[15]Loubeau, A. and Coulouvrat, F., "Effects of Meteorological Variability on Sonic Boom Propagation from Hypersonic Aircraft," *AIAA Journal*, Vol. 47, No. 11, 2009, pp. 2632–2641. doi:10.2514/1.41337.

[16]Ghanem, R. G. and Spanos, P. D., *Stochastic Finite Elements: A Spectral Approach*, Dover Publications, 2012.

[17]Holmes, P., Lumley, J. L., and Berkooz, G., *Turbulence, Coherent Structures, Dynamical Systems and Symmetry*, Cambridge Monographs on Mechanics, Cambridge University Press, 1996.

[18]Barth, T., "On the Calculation of Uncertainty Statistics with Error Bounds for CFD Calculations Containing Random Parameters and Fields," *Simulation Credibility: Advances in Verification, Validation, and Uncertainty Quantification*, edited by U. B. Mehta, D. R. Eklund, V. J. Romero, J. A. Pearce, and N. S. Keim, NASA TP—2016–219422 and JANNAF GL—2016–0001, 2016, pp. 211–248, https://www.nas.nasa.gov/assets/pdf/papers/NASA-TP-2016-219422_and_JANNAF-GL-2016-0001.pdf.

[19]Lorenz, E. N., "Empirical Orthogonal Functions and Statistical Weather Prediction," Statistical Forecasting Project, Department of Meteorology, MIT, Dec. 1956.

[20]Albert, S. W., Doostan, A., and Schaub, H., "Finite-Dimensional Density Representation for Aerocapture Uncertainty Quantification," AIAA Paper 2021-0932, Jan. 2021. doi:10.2514/6.2021-0932.

[21]Wang, X., Beller, L., Czado, C., and Holzapfel, F., "Modeling of Stochastic Wind Based on Operational Flight Data Using Karhunen–Loève Expansion Method," *Sensors*, Vol. 20, No. 16, 2020. doi:10.3390/s20164634.

[22]Nemec, M., Aftosmis, M. J., Rallabhandi, S. K., and Rodriguez, D. L., "Goal-Oriented Discretization Error Control in Coupled Nearfield-Farfield Low-Boom Simulations," AIAA Paper 2022-4085, June 2022. doi:10.2514/6.2022-4085.

[23]"Quesst Mission," https://www.nasa.gov/mission/quesst/, Accessed: 2024-06-07.

[24]Cleveland, R. O., *Propagation of Sonic Booms Through a Real, Stratified Atmosphere*, Ph.D. thesis, The University of Texas at Austin, 1995.

[25]Rallabhandi, S. K., "Advanced Sonic Boom Prediction Using the Augmented Burgers Equation," *J. Aircraft*, Vol. 48, No. 4, 2011, pp. 1245–1253. doi:10.2514/1.C031248.

[26]Yamamoto, M., Hashimoto, A., Aoyama, T., and Sakai, T., "A unified approach to an augmented Burgers equation for the propagation of sonic booms," *J. Acoust. Soc. Am.*, Vol. 137, No. 4, 2015, pp. 1857–1866. doi:10.1121/1.4916833.

[27]Hersbach, H., Bell, B., Berrisford, P., et al., "The ERA5 global reanalysis," *Quarterly Journal of the Royal Meteorological Society*, Vol. 146, No. 730, 2020, pp. 1999–2049. doi:https://doi.org/10.1002/qj.3803.

[28]Baudoin, M., Coulouvrat, F., and Thomas, J.-L., "Sound, infrasound, and sonic boom absorption by atmospheric clouds," *The Journal of the Acoustical Society of America*, Vol. 130, No. 3, 09 2011, pp. 1142–1153. doi:10.1121/1.3619789.

[29]Bradley, K. A., Hobbs, C. M., Wilmer, C. B., Sparrow, V. W., Stout, T. A., Morgenstern, J. M., Underwood, K. H., Maglieri, D. J., Cowart, R. A., Collmar, M. T., Shen, H., and Blanc-Benon, P., "Sonic Booms in Atmospheric Turbulence (SonicBAT): The Influence of Turbulence on Shaped Sonic Booms," NASA/CR 2020-220509, National Aeronautics and Space Administration, Center for AeroSpace Information, 7115 Standard Drive, Hanover, MD 21076, 2020, https://ntrs.nasa.gov/api/citations/20200002482/downloads/20200002482.pdf.

[30]Aftosmis, M. J., Berger, M. J., and Adomavicius, G., "A Parallel Multilevel Method for Adaptively Refined Cartesian Grids with Embedded Boundaries," AIAA Paper 2000–0808, Reno, NV, Jan. 2000.

[31]Aftosmis, M. J., Berger, M. J., and Murman, S. M., "Applications of Space-Filling-Curves to Cartesian Methods for CFD," AIAA Paper 2004–1232, Reno, NV, Jan. 2004.

[32]Nemec, M. and Aftosmis, M. J., "Toward Automatic Verification of Goal-Oriented Flow Simulations," NASA/TM 2014-218386, National Aeronautics and Space Administration, Center for AeroSpace Information, 7115 Standard Drive, Hanover, MD 21076, 2014, http://hdl.handle.net/2060/20150000864.

[33]Rodriguez, D. L., Aftosmis, M. J., and Nemec, M., "Formulation and Implementation of Inflow/Outflow Boundary Conditions to Simulate Propulsive Effects," AIAA Paper 2018-0334, Kissimmee, FL, Jan. 2018. doi:10.2514/6.2018-0334, AIAA SciTech Forum.

[34]"Automated Triangle Geometry Processing for Surface Modeling and Cartesian Grid Generation (Cart3D)," https://software.nasa.gov/software/ARC-14275-1, Accessed: 2024-06-07.

[35]Rallabhandi, S. K., Nielsen, E. J., and Diskin, B., "Sonic-Boom Mitigation Through Aircraft Design and Adjoint Methodology," *Journal of Aircraft*, Vol. 51, No. 2, 2014, pp. 502–510. doi:10.2514/1.C032189.

[36]"sBOOM2: An Advanced Sonic Boom Propagation and Design Tool," https://software.nasa.gov/software/LAR-20309-1, Accessed: 2024-06-07.

[37]Wintzer, M., Nemec, M., and Aftosmis, M. J., "Adjoint-Based Adaptive Mesh Refinement for Sonic Boom Prediction," AIAA Paper 2008-6593, August 2008.

[38]Anderson, G. R., Aftosmis, M. J., and Nemec, M., "Cart3D Simulations for the Second AIAA Sonic Boom Prediction Workshop," *Journal of Aircraft*, Vol. 56, No. 3, 2019, pp. 896–911. doi:10.2514/1.C034842.

[39]Spurlock, W. M., Aftosmis, M. J., and Nemec, M., "Cartesian Mesh Simulations for the Third AIAA Sonic Boom Prediction Workshop," *Journal of Aircraft*, Vol. 0, Article in Advance, pp. 1–17. doi:10.2514/1.C036405.

[40]"3rd AIAA Sonic Boom Prediction Workshop," https://lbpw.larc.nasa.gov/sbpw3, Accessed: 2024-06-07.

[41]Barth, T., "Non-intrusive Uncertainty Propagation with Error Bounds for Conservation Laws Containing Discontinuities," *Uncertainty Quantification in Computational Fluid Dynamics*, edited by H. Bijl, D. Lucor, S. Mishra, and C. Schwab, Springer, 2013.

[42]Barth, T., "An Overview of Combined Uncertainty and A-Posteriori Error Bound Estimates for CFD Calculations," AIAA Paper 2016-1062, Jan. 2016. doi:10.2514/6.2016-1062, 54th AIAA Aerospace Sciences Meeting.

[43]Barth, T., *QUEST Theory and Application Manual*, 4th ed., July 2023, NASA/SP-20230008157, https://ntrs.nasa.gov/api/citations/20230008157/downloads/8157.pdf.

[44]Clenshaw, C. W. and Curtis, A. R., "A method for numerical integration on an automatic computer," *Numer. Math.*, Vol. 2, 1960, pp. 197–205.

[45]Patterson, T. N. L., "The optimum addition of points to quadrature formulae," *Math. Comp.*, Vol. 22, 1968, pp. 847–856.

[46]World Meteorological Organization, *Guide to Meteorological Instruments and Methods of Observation, WMO-No. 8*, 7th ed., ANNEX 4.B.